This is a repository copy of *Chiral topological add–drop filter for integrated quantum photonic circuits*.

White Rose Research Online URL for this paper:
https://eprints.whiterose.ac.uk/199628/

Version: Published Version

eprints@whiterose.ac.uk
https://eprints.whiterose.ac.uk/

OPTICA

Chiral topological add–drop filter for integrated quantum photonic circuits

M. Jalali Mehrabad,[1,2,5] A. P. Foster,[1,3] N. J. Martin,[1,*] R. Dost,[1] E. Clarke,[4]
P. K. Patil,[4] M. S. Skolnick,[1] and L. R. Wilson[1]

[1]*Department of Physics and Astronomy, University of Sheffield, Sheffield S3 7RH, UK*
[2]*Current address: Joint Quantum Institute, University of Maryland, College Park, Maryland 20742, USA*
[3]*Current address: Aegiq Ltd, Cooper Buildings, Arundel Street, Sheffield S1 2NS, UK*
[4]*EPSRC National Epitaxy Facility, University of Sheffield, Sheffield S1 4DE, UK*
[5]*mjalalim@umd.edu*
*nmartin3@sheffield.ac.uk

The integration of quantum emitters within topological nanophotonic devices enables the control of light–matter interactions at the single photon level. Here, we experimentally realize an integrated topological add–drop filter and observe multiport chiral emission from single photon emitters (quantum dots) embedded within the device. The filter is imprinted within a valley-Hall photonic crystal membrane and comprises a resonator evanescently coupled to a pair of access waveguides. We show that the longitudinal modes of the resonator enable the filter to perform wavelength-selective routing of light, protected by the underlying topology. Furthermore, we demonstrate that for a quantum dot located at a chiral point in the resonator, selective coupling occurs between well-defined spin states and specific pairs of the filter output ports. The combination of multiport routing, allied with the inherent nonreciprocity of the device at the single photon level, presents opportunities for the formation of complex quantum optical devices, such as an on-chip quantum optical circulator.

1. INTRODUCTION

Photonic crystals (PhCs) constitute a well-established component in nanophotonic circuitry, their subwavelength features supporting low-loss routing of on-chip light within a compact device footprint. Recently, the translation of concepts from the field of topological insulators to the photonic domain has provided new mechanisms for nanoscale control and manipulation of light within the PhCs. Notably, photonic analogs of the spin-Hall [1] and valley-Hall [2] effects have been developed; significant advantages of these approaches include robust, wavelength independent transport of light around tight bends, and the potential to form chiral light–matter interfaces in combination with embedded quantum emitters. Devices containing topological photonic interfaces have been demonstrated experimentally using both spin- and valley-Hall PhCs, predominantly in the silicon [3,4] and GaAs [5–10] material platforms. In particular, we note that bend robustness has been well established [3–5,9,11–13] and leveraged to form PhC topological ring resonators [6–8,14].

Due to their preservation of time-reversal symmetry, both spin- and valley-Hall photonic analogs support degenerate counter-propagating interface modes, unlike their electronic counterparts. Nevertheless, the modes can be rendered unidirectional by spin selection. At locations known as chiral points, the counterpropagating modes of a topological waveguide have orthogonal circular polarization. A circularly polarized emitter placed at such a point interacts uniquely with the mode with equivalent handedness, and therefore orthogonal circularly polarized dipoles emit in opposite directions; this is the basis of a chiral light–matter interface [15,16]. Semiconductor quantum dots (QDs), which have subnanosecond radiative lifetimes and have been shown to emit single photons with near-transform limited linewidths [17,18], are a leading "matter" candidate in this regard; chiral interfaces have been demonstrated using QDs coupled to both spin-Hall [5] and valley-Hall [6,8] PhC waveguides. These works built upon substantial prior achievements in topologically trivial chiral systems; for instance, those using atoms coupled to microresonators [19,20] and QDs embedded in nanobeam [21,22] or glide plane PhC [23] waveguides.

The field of on-chip topological quantum photonics is seeing rapid progress; for example, manipulation of the quantum states of light has been demonstrated using relatively large topological photonic waveguide devices [24–27], while at the nanoscale a passive topological PhC device was recently used as the basis for a simple quantum photonic circuit [28]. In contrast, the development of topological photonic devices with integrated quantum emitters

is still very much in its infancy. Here, we combine the compactness and chirality afforded by topology to demonstrate chiral emission from a QD embedded in a valley-Hall PhC add–drop filter (ADF) comprising a resonator and pair of access waveguides. Ridge waveguides used for conventional ADFs based on microresonators do not provide the same favorable conditions that can be achieved with the incorporation of quantum emitters using PhC waveguides. However, proposed designs for conventional, topologically trivial PhC ADFs, while possessing favorable conditions for integrated quantum emitters such as enhanced light–matter interaction from slow light, Stark tuning and chiral emission, have nonideal fundamental device operation including single-mode operation and increased loss [29]. It is possible, however, to overcome the limitations of these approaches by using topological protection, allowing (1) reduced reflections and scattering, (2) the realization of multimode operation, and (3) the fine control of coupling between the waveguide and resonator, within the ADF.

We first demonstrated that the device supports wavelength-dependent light routing. Then, we observed chiral emission from a QD coupled spatially and spectrally to a resonator mode. In the latter measurement, photons emitted after recombination of a specific QD spin state are coupled into two of the four output modes of the device; the chiral nature of the light–matter interface results in the orthogonal spin state coupling to the other two output modes. Potential applications of the ADF include all-optical logic gates [30], boson sampling [31], and filtering/routing [32] and demultiplexing of single photons [33], as well as linear optical quantum computing [34,35]. Additionally, the nonreciprocity inherent in our compact, multiport integrated device is essential for the realization of devices such as an on-chip quantum optical circulator [36].

2. VALLEY-HALL RESONATOR DESIGN

Our integrated nanophotonic device is configured within a 2D PhC that has valley-Hall-type topology. The rhombic unit cell of the PhC comprises two equilateral triangular apertures, which are formed within a thin, freestanding dielectric membrane. We evaluate the TE band structure of the PhC using the freely available MPB software package [37]. When the apertures are of equal size, the TE band structure exhibits a Dirac cone at the K point, as shown in Fig. 1(a). Expanding one aperture while shrinking the other, however, leads to the opening of a topological bandgap at the K point, which is also shown in Fig. 1(a). We can then take advantage of the topological bulk-edge correspondence to realize within the PhC a waveguide that supports a topologically nontrivial optical mode. To achieve this, we break the inversion symmetry of the PhC by inverting the unit cells in one half of the PhC, creating a zigzag interface at the boundary between the two regions comprising inverted (labeled VPC1) and uninverted (VPC2) unit cells, respectively. Two possible zigzag interfaces can be formed in this way, characterized by the proximity of either the large or small triangular apertures at the boundary of VPC1 and VPC2 unit cells. We refer to these as type A and type B interfaces, respectively, as shown in Fig. 1(b). The associated dispersion diagram shows that both interfaces support a single guided TE mode, which extends across 100% (∼84%) of the bandgap for the type A (B) interface.

Two defining characteristics of valley-Hall topologically nontrivial optical modes are (i) their broadband ability to navigate sharp corners without experiencing backscatter (due to the suppression of intervalley scattering, a result of the vanishing field overlapping between the two valley states [12]) and (ii) the helical nature of the modes. These properties are critical to the operation
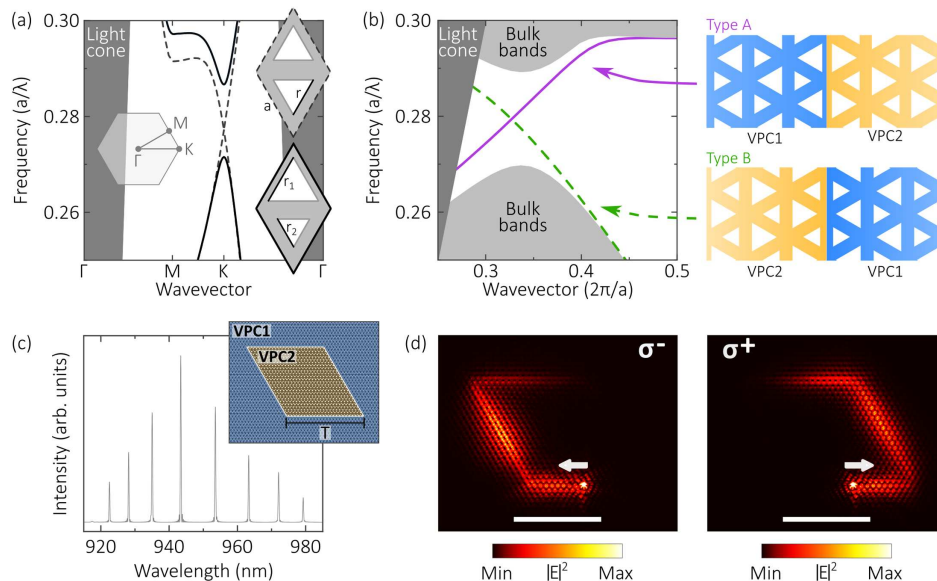

Fig. 1. (a) Band diagram for a triangular lattice PhC formed using either unperturbed (dashed line) or perturbed (solid line) rhombic unit cells. Insets show (left) the first Brillouin zone and (right) schematics of the unit cells, with equilateral triangles representing air holes in a dielectric membrane. The triangle side lengths are $(r, r_1, r_2) = (0.5a, 0.4a, 0.6a)$, where a is the lattice constant. The membrane has a thickness of $h = 0.64a$ and refractive index $n = 3.4$. (b) TE dispersion diagram for two possible zigzag interfaces formed by inverting the unit cells in one half of the PhC. These are labeled type A and type B in the accompanying schematics. (c) Simulated mode spectrum for a rhombic ring resonator formed using the topological zigzag interface. The resonator has a side length of $T = 20$ unit cells and lattice period $a = 266$ nm. A schematic of the resonator is shown in the inset. (d) Simulated, spatially resolved electric field intensity when a resonator mode is excited by a dipole positioned at a chiral point on the interface. The dipole is either (left) σ^- or (right) σ^+ polarized. The approximate location of the dipole sources for the two simulations is given by the white dot within the figures, with the dipole sources being located at a chiral point shown in the S_3 maps of Fig. S1 in Supplement 1. The electric field intensities are averaged over the first 200 fs of simulation time. Arrows indicate the direction of light propagation in each case. Scale bars: 4 µm.

of the photonic device reported here. To demonstrate the backscatter protection afforded by topology to the waveguide mode, we used finite-difference time-domain (FDTD) simulations [38] to probe the optical properties of a rhombus-shaped ring resonator, formed by embedding VPC2 unit cells inside a larger VPC1 unit cell matrix, as shown in Fig. 1(c). In this structure, a bend with a 60 (120) deg internal angle connects interfaces of differing (the same) type, giving a maximum resonator spectral bandwidth of ∼84% of the bandgap, following from the discussion above. The device parameters used in Fig. 1(c) are chosen to enable operation in the near IR (NIR), compatible with the highest quality QDs and the spectral region in which our later experiments are conducted.

The resulting mode spectrum reveals clear longitudinal modes lying within the topological bandgap (∼920 − 980 nm), with Q factors on the order of 10^5 for a resonator side length of $T = 20$ unit cells, with the main limiting factor for this simulated Q factor being out-of-plane scattering. Significantly, the predicted device performance is broadband in nature, indicating that topological protection overcomes the wavelength dependence commonly observed in light transmission through topologically trivial PhC waveguide bends. Further evidence of topological protection can be found in Fig. 1(d), in which we excite the resonator using a circularly polarized dipole source. By suitable positioning of the dipole at a chiral point (see Supplement 1, Section S1) a single unidirectional mode is excited, which travels either clockwise (CW) or counterclockwise (CCW) around the ring, depending on the handedness of the source polarization. The mode is seen to navigate the resonator corners smoothly and without backscattering. This simulation also serves to highlight the second key element of our device: the potential to realize a unidirectional light–matter interaction between a resonator mode and an embedded quantum emitter, which ultimately enables spin-dependent routing of on-chip light. This high chiral contrast and wavelength independent operation is made possible by the topological protection valley-Hall waveguides exhibit, with the topological trivial case unable to operate in this way [8].

3. TOPOLOGICAL ADD-DROP FILTER

To enable integration of the resonator within scalable nanophotonic circuits, we introduced parallel "bus" and "drop" access waveguides in close proximity to the opposing sides of the rhombus-shaped resonator, forming an ADF. The filter is shown schematically in Fig. 2(a). Evanescent coupling between waveguides and resonator in this geometry enables light to enter (exit) the resonator from (into) the waveguides. Geometrically, the coupling strength is dependent on the waveguide-resonator coupling length L and separation S. In our structure, bends in each waveguide allow these parameters to be decoupled, providing increased flexibility in device design. The effect of changing S is investigated in Supplement 1, Section S2.

The optical properties of the device are demonstrated using an FDTD simulation in which broadband light is injected using a chiral source embedded in the bus waveguide, and the power subsequently transmitted through the bus waveguide or coupled into the drop waveguide is monitored. Note that the through and dropped signals propagate in opposite directions due to a combination of valley momentum conservation and the use of both type A and B interfaces in the device. (This is examined in detail in Supplement 1, Section S3.) The simulation results are summarized in Figs. 2(b)–2(d), with mode resonances clearly visible in the data. We first note that off-resonance, the through transmission approaches unity and the dropped signal is strongly suppressed, with an extinction ratio of 18–22 dB at the midpoint between adjacent modes. Conversely, clear transmission minima in the through direction are observed at wavelengths that correspond to the longitudinal modes of the resonator. These minima occur due to destructive interference between the two possible pathways for light to exit the device in the through direction (either directly along the bus waveguide or via the resonator). Corresponding maxima are seen in the drop channel output, showing that light is transferred from input to drop waveguide when resonant with a ring mode. The degree to which the input light is dropped depends on the waveguide-resonator coupling strength, with critical coupling occurring for $S \sim 4 - 8$ unit cells (mode dependent). For the device simulated here, the loaded modal Q factors lie in the 400–1600 range, with extinction ratios (drop signal to through signal) of 11–21 dB. In Supplement 1 we show that the ADF performance is robust against certain defects, and present an exemplary use of the passive filter to realize robust, compact on-chip optical logic gates (Supplement 1, Sections S4–S7).

We fabricated the topological ADF experimentally within a nominally 170 nm thin GaAs membrane, which contains a single layer of InAs QDs within the diode's intrinsic region. A 1.15 µm thick AlGaAs sacrificial layer beneath the membrane is removed
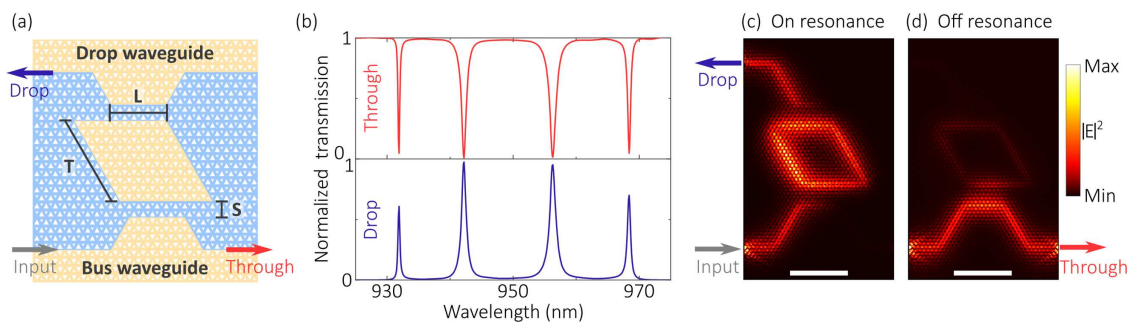

Fig. 2. (a) Schematic of the topological ADF, with PhC unit cells color-coded as in Fig. 1(b) by orientation (inverted (VPC1) or uninverted (VPC2)). (b) Simulated transmission in the through (lower right) and drop (upper left) directions for an ADF with $T = 16$, $S = 6$, and $L = 11$ unit cells, respectively. The data is normalized to the bus waveguide transmission in the absence of the resonator, with the power measured within the confines of the PhC structure.(c) Time-averaged electric field intensity for light input on resonance with the longitudinal mode at 955 nm. (d) Time-averaged electric field intensity when the input is off resonance (969 nm). Scale bars in (c) and (d) are 4 µm. The light source is located within a nanobeam waveguide connected to the input port, at the point indicated by the gray arrow.
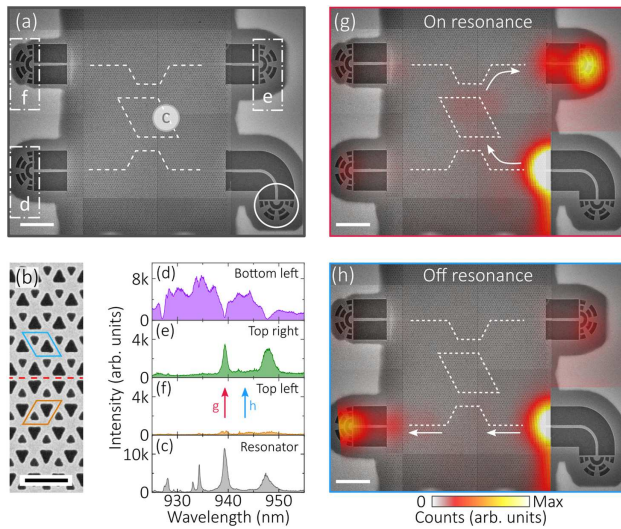
Fig. 3. (a) SEM image of a topological ADF, with waveguide–resonator separation $S = 6$ unit cells. The topological interfaces forming the waveguides and resonator are highlighted by dashed white lines. (b) Higher magnification SEM image of a type A interface (red dashed line). Unit cells on either side of the interface are outlined. Scale bar: 500 nm. (c) PL spectrum acquired by exciting the QD ensemble at the resonator interface and collecting emission from the lower right OC [open white circle in (a)]. (d–f) PL spectra acquired by exciting the QD ensemble in the lower right OC and collecting emission independently from the other three OCs. The collection position in each case is given in (a). (g–h) Integrated PL intensity as a function of collection position, overlaid on an SEM image of the device. The excitation is fixed above the lower right OC. The integration is taken over (g) 939.3 nm to 939.5 nm and (h) 943 nm to 944 nm, respectively. The waveguide and resonator interfaces are identified using white dashed lines, while arrows provide a guide to the the direction of light transmission. Data from above the excitation location (lower right corner) has been omitted, and the zero of the color scale has been made transparent to aid visualization of the device. Scale bars in (a), (g), and (h): 4 μm.

to create a freestanding structure. Details of the fabrication procedure can be found in Section 4 (Methods). A SEM image of a representative device is shown in Fig. 3(a). Note that each output of the ADF is coupled to a nanobeam waveguide, which is terminated using a grating outcoupler (OC) for efficient coupling of light into free space optics. A higher magnification SEM image of a type A interface is shown in Fig. 3(b).

To demonstrate the basic operation of the ADF, we first evaluated the mode spectrum of the device by measuring high-power photoluminescence (PL) from the QD ensemble located within the resonator, as shown in Fig. 3(c). Quality (Q) factors of 1100 and 440 are obtained for the modes at 939 nm and 947 nm, respectively, in good agreement with the range of values obtained from the simulation. We then injected broadband light into the lower waveguide via high-power, nonresonant excitation of the QD ensemble in the bottom right OC, and measured the resulting signal from the through and drop ports (bottom left and top right OCs, respectively). The resulting spectra are shown in Figs. 3(d) and 3(e). For completeness, we also detected the output from the OC in the top left of the device, and the data is shown in Fig. 3(f).

Considering the signal transmitted through the bus waveguide [Fig. 3(d)], we observed several strong dips in transmission that are resonant with the longitudinal modes of the resonator. Indeed, for three of the four modes, the transmission is almost completely

inhibited. Note that spectrally dependent intensity variations occur in these measurements due to the use of quasi-broadband PL from many different QDs. In the drop direction [Fig. 3(e)], corresponding peaks are observed for the modes at 939 nm and 947 nm, showing that at these wavelengths, light is coupled from the bus to the drop waveguide via the resonator. Importantly, we see only very weak emission from the other end of the drop waveguide [Fig. 3(f)], demonstrating suppression of backscatter around the sharp bends of the topological resonator.

Next, we focused our attention on the mode centered at ~939 nm, resonant with which the transmission of the bus waveguide approaches zero (suggestive of critical coupling). We stepped the collection spot in an $x − y$ grid across the device while the excitation laser remains fixed above the lower right OC, and acquire a PL spectrum at each grid position. The resulting data is spectrally filtered such that it corresponds to either on or off resonance with the longitudinal mode at ~939 nm. Spatial maps giving the integrated PL signal are shown in Figs. 3(g) and 3(h). On resonance, light is detected predominantly from the drop (top right) OC, showing that it is coupled through the resonator. Conversely, when off-resonant the largest signal is from the left-hand OC of the bus waveguide, bypassing the resonator. Scattering is also observed at the nanobeam-topological waveguide interfaces, which were not optimized in this device. More significantly, minimal scattering is observed from above the bends in the topological interface, testifying to their quality. A complementary measurement in which the excitation location was scanned while PL emission was collected from a single fixed OC is presented in Supplement 1, Section S6.

Having demonstrated the basic function of the device, next we considered a second operational paradigm, in which we utilized single QDs embedded at the resonator interface. We first performed a Hanbury Brown and Twiss (HBT) measurement on photons emitted from a QD that is coupled spectrally and spatially to a resonator mode. In so doing, we collected light into separate optical fibers from either end of one bus waveguide, therefore performing the HBT beam-splitting operation on chip (see Supplement 1, Section S7). We obtained a $g^{(2)}(0)$ of 0.14 after correcting for background emission from other QDs coupled to the same resonator mode, demonstrating the single photon nature of the QD emission.

Next, we investigated the chiral behavior of a single QD in a similar device. A schematic of the structure and the measured resonator spectrum are shown in Fig. 4(a) and Fig. 4(b), respectively. The QD is excited nonresonantly and PL emission is subsequently detected from all four ports of the ADF. The resulting spectra as a function of the magnetic field are shown in Figs. 4(c)–4(f). Clear routing of light dependent on the spin state of the QD transition is observed. First, we considered the spectra obtained at $B_z = 0$ T, for which the two spin states of the QD transition are degenerate, and note that a single PL emission line is observed from all output ports. Due to the statistical emission from both spin states of the QD, the source in this case is effectively unpolarized and therefore excites both CW and CCW resonator modes, which subsequently decay equally into the four output ports.

However, upon application of a magnetic field in the Faraday geometry, the Zeeman effect leads to spin splitting, giving rise to two nondegenerate, orthogonal, circularly polarized QD transitions. For a suitably positioned emitter, spin-momentum locking at the topological interface ensures that the direction of emission from the QD is dependent on the spin state. One of the spin states
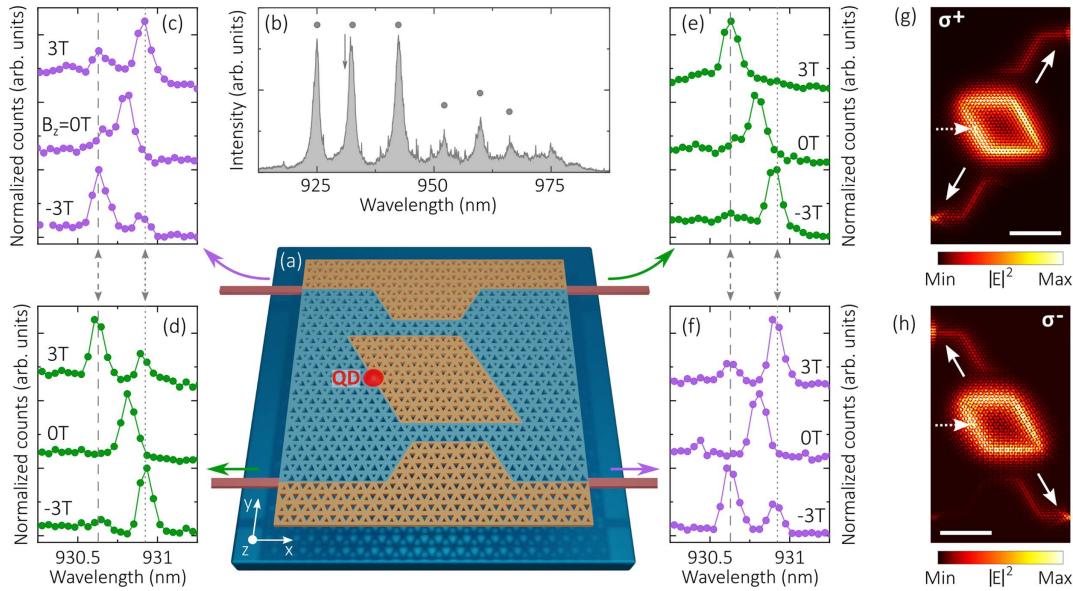
Fig. 4. (a) Schematic of the ADF, with a QD embedded at the resonator interface. Each of the four nanobeam waveguides is terminated with a grating outcoupler (OC), not shown. (b) PL spectrum acquired from an OC under high-power excitation of the resonator interface. The longitudinal resonator modes are marked by filled circles. The device parameters are $(T, S, L) = (16, 10, 11)$ unit cells, respectively. (c–f) Low-power PL spectra for a single QD located at the resonator interface and with an optical transition near-resonant with a longitudinal mode [see arrow in (b)]. The spectra are acquired from the OCs in, respectively, (c) the top left, (d) the lower left, (e) the top right, and (f) the lower right of the device. Data is shown for three different magnetic field strengths, $B_z = -3$ T, 0 T, and 3 T. Dashed and dotted lines indicate the approximate wavelengths of the two QD transitions under a nonzero magnetic field. (g–h) Simulated, time-averaged electric field intensity in the plane of the device, for a (g) σ^+ or (h) σ^- polarized dipole placed at a chiral point at the resonator interface (approximate location given by the dashed arrow, with the dipole source located at a chiral point shown in the S_3 maps of Fig. S1 in Supplement 1). Solid arrows indicate the dominant coupling directions from of the resonator in each case. Scale bars: 4 µm.

therefore couples to the CW resonator mode, while the other spin state couples to the CCW mode. The modes subsequently decay directionally into the two waveguides. Valley-momentum conservation results in a single resonator mode coupling to diagonally opposing ports of the ADF; therefore, a single QD spin state also couples in the same manner in our device. For instance, at a magnetic field of 3 T the dominant emission line measured from the top left and lower right OCs is at a longer wavelength, while the opposite is true for the other two OCs. When the sign of the magnetic field is flipped, the situation is reversed, with the shorter wavelength peak becoming dominant in the top left and lower right data. Thus, the device acts as a bidirectional chiral router for each spin state of the QD. FDTD simulations for σ^+ and σ^- dipoles placed at the resonator interface support the experimental observation [Figs. 4(g) and 4(h)]. We note a high, but not unity chiral, contrast for this QD, explained most likely by a slight deviation from the peak of the chiral maps shown in Fig. S1 in Supplement 1. We also noted that the direction of travel of the spin state will change depending on the location of the QD within the chiral map. Additional experimental data is shown in Supplement 1, Section S8 for a second QD coupled to a different mode of the same device, demonstrating the broadband potential of the structure.

4. METHODS

A. Device Fabrication

The device layers were grown on a semi-insulating (100) GaAs substrate using molecular beam epitaxy. In the order of deposition, the layers are: 1 µm $Al_{0.6}Ga_{0.4}As$, 30 nm n-GaAs, 50 nm $Al_{0.3}Ga_{0.7}As$,

5 nm i-GaAs, InAs QDs, 5 nm i-GaAs, 30 nm $Al_{0.3}Ga_{0.7}As$, and 50 nm p-GaAs.

Nanophotonic devices were fabricated using standard lithography and wet/dry etching techniques. A 120 nm thick SiO_x hardmask was deposited on the wafer using plasma-enhanced chemical vapor deposition. This was followed by the spinning of an electron-beam-sensitive resist (CSAR). The devices were subsequently patterned using 50 kV electron beam lithography (Raith Voyager) and then etched into the hardmask and epitaxial layers using, respectively, reactive ion etching (RIE) and inductively coupled plasma RIE. The hardmask and AlGaAs sacrificial layer were removed using a hydrofluoric acid wet etch.

B. Experimental Methods

The sample was mounted in a superconducting magnet cryostat (Cryo Industries of America) operating at 4.2 K. PL measurements were undertaken using nonresonant laser excitation at 770 nm (SolsTiS, M Squared). For the creation of spatial PL maps, the excitation or collection spot was rastered across the sample using a motorized mirror in the microscope excitation or collection path. The use of a relay lens pair ensured that the laser and collection spots remained well-focused across the full scanning range during this process.

For autocorrelation (HBT) measurements, the sample was excited using an 808 nm diode laser (CPS808, Thorlabs). The signal was collected independently from either end of one bus waveguide, and coupled into separate optical fibers. Two 0.75 m monochromators (SP-2750, Princeton Instruments) were used to filter the output (filter bandwidth ~0.1 nm), which was then detected using two avalanche photodiodes (SPCM, Excelitas) with

a convolved instrument response time of $\sim$700 ps. Photon arrival times were recorded and time-correlated using two channels of a time tagger (TimeTagger Ultra, Swabian Instruments).

5. DISCUSSION AND CONCLUSION

We have demonstrated an integrated topological add–drop filter operating in the optical domain. The filter consists of a compact resonator coupled to a pair of access waveguides, defined within a valley-Hall topological PhC. Characterization of the device using broadband emission from the QD ensemble indicates that near-critical coupling between the waveguides and resonator was achieved, allied with suppressed scatter, both in and out of the plane. Chiral emission from a QD embedded within the resonator was also demonstrated. One spin state of a QD transition was shown to couple into two of the four output ports of the device, with the orthogonal spin state coupling to the other two output ports.

In future work, optimization of the device to increase the intrinsic (unloaded) resonator Q factor could enable broadband Purcell enhancement [39] of the chiral light–matter interaction, as recently demonstrated for a non-chiral device [40]. This might be achieved, for instance, by passivation of the semiconductor surface to suppress surface-related losses [39,41,42]. Scale up could then be envisioned; for example, cascaded chiral resonators could be used for the transport of on-chip entangled states [43]. Furthermore, addressing the QD resonantly in the coherent scattering regime [44,45] could ultimately allow for the realization of a topologically protected, integrated quantum optical circulator [36].

Disclosures. The authors declare no conflicts of interest.

Data availability. The data that support the plots within this paper and other findings of this study are available from the corresponding author upon reasonable request.

Supplemental document. See Supplement 1 for supporting content.

REFERENCES

1. L.-H. Wu and X. Hu, "Scheme for achieving a topological photonic crystal by using dielectric material," Phys. Rev. Lett. **114**, 223901 (2015).
2. T. Ma and G. Shvets, "All-Si valley-Hall photonic topological insulator," New J. Phys. **18**, 025012 (2016).
3. N. Parappurath, F. Alpeggiani, L. Kuipers, and E. Verhagen, "Direct observation of topological edge states in silicon photonic crystals: spin, dispersion, and chiral routing," Sci. Adv. **6**, eaaw4137 (2020).
4. M. I. Shalaev, W. Walasik, A. Tsukernik, Y. Xu, and N. M. Litchinitser, "Robust topologically protected transport in photonic crystals at telecommunication wavelengths," Nat. Nanotechnol. **14**, 31 (2019).
5. S. Barik, A. Karasahin, C. Flower, T. Cai, H. Miyake, W. DeGottardi, M. Hafezi, and E. Waks, "A topological quantum optics interface," Science **359**, 666 (2018).
6. S. Barik, A. Karasahin, S. Mittal, E. Waks, and M. Hafezi, "Chiral quantum optics using a topological resonator," Phys. Rev. B **101**, 205303 (2020).
7. M. J. Mehrabad, A. P. Foster, R. Dost, E. Clarke, P. K. Patil, I. Farrer, J. Heffernan, M. S. Skolnick, and L. R. Wilson, "A semiconductor topological photonic ring resonator," Appl. Phys. Lett. **116**, 061102 (2020).
8. M. J. Mehrabad, A. P. Foster, R. Dost, E. Clarke, P. K. Patil, A. M. Fox, M. S. Skolnick, and L. R. Wilson, "Chiral topological photonics with an embedded quantum emitter," Optica **7**, 1690–1696 (2020).
9. T. Yamaguchi, Y. Ota, R. Katsumi, K. Watanabe, S. Ishida, A. Osada, Y. Arakawa, and S. Iwamoto, "GaAs valley photonic crystal waveguide with light-emitting InAs quantum dots," Appl. Phys. Express **12**, 062005 (2019).
10. H. Yoshimi, T. Yamaguchi, Y. Ota, Y. Arakawa, and S. Iwamoto, "Slow light waveguides in topological valley photonic crystals," Opt. Lett. **45**, 2648–2651 (2020).
11. J. Ma, X. Xi, and X. Sun, "Topological photonic integrated circuits based on valley kink states," Laser Photon. Rev. **13**, 1900087 (2019).
12. X.-T. He, E.-T. Liang, J.-J. Yuan, H.-Y. Qiu, X.-D. Chen, F.-L. Zhao, and J.-W. Dong, "A silicon-on-insulator slab for topological valley transport," Nat. Commun. **10**, 872 (2019).
13. H. Yoshimi, T. Yamaguchi, R. Katsumi, Y. Ota, Y. Arakawa, and S. Iwamoto, "Experimental demonstration of topological slow light waveguides in valley photonic crystals," Opt. Express **29**, 13441–13450 (2021).
14. L. Gu, Q. Yuan, Q. Zhao, Y. Ji, Z. Liu, L. Fang, X. Gan, and J. Zhao, "A topological photonic ring-resonator for on-chip channel filters," J. Lightwave Technol. **39**, 5069–5073 (2021).
15. A. B. Young, A. C. T. Thijssen, D. M. Beggs, P. Androvitsaneas, L. Kuipers, J. G. Rarity, S. Hughes, and R. Oulton, "Polarization engineering in photonic crystal waveguides for spin-photon entanglers," Phys. Rev. Lett. **115**, 153901 (2015).
16. P. Lodahl, S. Mahmoodian, S. Stobbe, A. Rauschenbeutel, P. Schneeweiss, J. Volz, H. Pichler, and P. Zoller, "Chiral quantum optics," Nature **541**, 473–480 (2017).
17. A. V. Kuhlmann, J. H. Prechtel, J. Houel, A. Ludwig, D. Reuter, A. D. Wieck, and R. J. Warburton, "Transform-limited single photons from a single quantum dot," Nat. Commun. **6**, 8204 (2015).
18. F. T. Pedersen, Y. Wang, C. T. Olesen, S. Scholz, A. D. Wieck, A. Ludwig, M. C. Lobl, R. J. Warburton, L. Midolo, R. Uppu, and P. Lodahl, "Near transform-limited quantum dot linewidths in a broadband photonic crystal waveguide," ACS Photon. **7**, 2343 (2020).
19. C. Junge, D. O'Shea, J. Volz, and A. Rauschenbeutel, "Strong coupling between single atoms and nontransversal photons," Phys. Rev. Lett. **110**, 213604 (2013).
20. S. Rosenblum, O. Bechler, I. Shomroni, Y. Lovsky, G. Guendelman, and B. Dayan, "Extraction of a single photon from an optical pulse," Nat. Photonics **10**, 19–22 (2016).
21. I. J. Luxmoore, N. A. Wasley, A. J. Ramsay, A. C. T. Thijssen, R. Oulton, M. Hugues, S. Kasture, V. G. Achanta, A. M. Fox, and M. S. Skolnick, "Interfacing spins in an InGaAs quantum dot to a semiconductor waveguide circuit using emitted photons," Phys. Rev. Lett. **110**, 037402 (2013).
22. R. J. Coles, D. M. Price, J. E. Dixon, B. Royall, E. Clarke, P. Kok, M. S. Skolnick, A. M. Fox, and M. N. Makhonin, "Chirality of nanophotonic waveguide with embedded quantum emitter for unidirectional spin transfer," Nat. Commun. **7**, 11183 (2016).
23. I. Söllner, S. Mahmoodian, S. L. Hansen, L. Midolo, A. Javadi, G. Kiršanskè, T. Pregnolato, H. El-Ella, E. H. Lee, J. D. Song, S. Stobbe, and P. Lodahl, "Deterministic photon-emitter coupling in chiral photonic circuits," Nat. Nanotechnol. **10**, 775 (2015).
24. J.-L. Tambasco, G. Corrielli, R. J. Chapman, A. Crespi, O. Zilberberg, R. Osellame, and A. Peruzzo, "Quantum interference of topological states of light," Sci. Adv. **4**, eaat3187 (2018).
25. Y. Wang, X.-L. Pang, Y.-H. Lu, J. Gao, Y.-J. Chang, L.-F. Qiao, Z.-Q. Jiao, H. Tang, and X.-M. Jin, "Topological protection of two-photon quantum correlation on a photonic chip," Optica **6**, 955–960 (2019).
26. A. Blanco-Redondo, B. Bell, D. Oren, B. J. Eggleton, and M. Segev, "Topological protection of biphoton states," Science **362**, 568 (2018).
27. S. Mittal, V. V. Orre, E. A. Goldschmidt, and M. Hafezi, "Tunable quantum interference using a topological source of indistinguishable photon pairs," Nat. Photonics **15**, 542–548 (2021).
28. Y. Chen, X.-T. He, Y.-J. Cheng, H.-Y. Qiu, L.-T. Feng, M. Zhang, D.-X. Dai, G.-C. Guo, J.-W. Dong, and X.-F. Ren, "Topologically protected valley-dependent quantum photonic circuits," Phys. Rev. Lett. **126**, 230503 (2021).
29. M. Bazian, "Photonic crystal add-drop filter: a review on principles and applications," Photon. Netw. Commun. **41**, 57 (2021).

30. L. He, W. X. Zhang, and X. D. Zhang, "Topological all-optical logic gates based on two-dimensional photonic crystals," Opt. Express **27**, 25841–25859 (2019).

31. H. Wang, Y. He, Y.-H. Li, Z.-E. Su, B. Li, H.-L. Huang, X. Ding, M.-C. Chen, C. Liu, J. Qin, J.-P. Li, Y.-M. He, C. Schneider, M. Kamp, C.-Z. Peng, S. Höfling, C.-Y. Lu, and J.-W. Pan, "High-efficiency multiphoton boson sampling," Nat. Photonics **11**, 361–365 (2017).

32. S. Aghaeimeibodi, J.-H. Kim, C.-M. Lee, M. A. Buyukkaya, C. Richardson, and E. Waks, "Silicon photonic add-drop filter for quantum emitters," Opt. Express **27**, 16882–16889 (2019).

33. F. Lenzini, B. Haylock, J. C. Loredo, R. A. Abrahão, N. A. Zakaria, S. Kasture, I. Sagnes, A. Lemaitre, H.-P. Phan, D. V. Dao, P. Senellart, M. P. Almeida, A. G. White, and M. Lobino, "Active demultiplexing of single photons from a solid-state source," Laser Photon. Rev. **11**, 1600297 (2017).

34. J. Carolan, C. Harrold, C. Sparrow, E. Martín-López, N. J. Russell, J. W. Silverstone, P. J. Shadbolt, N. Matsuda, M. Oguma, M. Itoh, G. D. Marshall, M. G. Thompson, J. C. F. Matthews, T. Hashimoto, J. L. O'Brien, and A. Laing, "Universal linear optics," Science **349**, 711 (2015).

35. N. C. Harris, D. Grassani, A. Simbula, M. Pant, M. Galli, T. Baehr-Jones, M. Hochberg, D. Englund, D. Bajoni, and C. Galland, "Integrated source of spectrally filtered correlated photons for large-scale quantum photonic systems," Phys. Rev. X **4**, 041047 (2014).

36. M. Scheucher, A. Hilico, E. Will, J. Volz, and A. Rauschenbeutel, "Quantum optical circulator controlled by a single chirally coupled atom," Science **354**, 1577 (2016).

37. S. G. Johnson and J. D. Joannopoulos, "Block-iterative frequency-domain methods for Maxwell's equations in a planewave basis," Opt. Express **8**, 173–190 (2001).

38. Ansys Lumerical, https://www.ansys.com/products/photonics.

39. X. Xie, S. Yan, J. Dang, J. Yang, S. Xiao, Y. Wang, S. Shi, L. Yang, D. Dai, Y. Yuan, N. Luo, T. Cui, G. Chi, Z. Zuo, B.-B. Li, C. Wang, and X. Xu, "Topological cavity based on slow-light topological edge mode for broadband Purcell enhancement," Phys. Rev. Appl. **16**, 014036 (2021).

40. L. Dusanowski, D. Köck, E. Shin, S.-H. Kwon, C. Schneider, and S. Höfling, "Purcell-enhanced and indistinguishable single-photon generation from quantum dots coupled to on-chip integrated ring resonators," Nano Lett. **20**, 6357–6363 (2020).

41. B. Guha, F. Marsault, F. Cadiz, L. Morgenroth, V. Ulin, V. Berkovitz, A. Lemaître, C. Gomez, A. Amo, S. Combrié, B. Gérard, G. Leo, and I. Favero, "Surface-enhanced gallium arsenide photonic resonator with quality factor of 6x10^6," Optica **4**, 218–221 (2017).

42. K. Kuruma, Y. Ota, M. Kakuda, S. Iwamoto, and Y. Arakawa, "Surface-passivated high-Q GaAs photonic crystal nanocavity with quantum dots," APL Photon. **5**, 046106 (2020).

43. W.-K. Mok, D. Aghamalyan, J.-B. You, T. Haug, W. Zhang, C. E. Png, and L.-C. Kwek, "Long-distance dissipation-assisted transport of entangled states via a chiral waveguide," Phys. Rev. Res. **2**, 013369 (2020).

44. D. Rattenbacher, A. Shkarin, J. Renger, T. Utikal, S. Götzinger, and V. Sandoghdar, "Coherent coupling of single molecules to on-chip ring resonators," New J. Phys. **21**, 062002 (2019).

45. A. Brooks, X.-L. Chu, Z. Liu, R. Schott, A. Ludwig, A. D. Wieck, L. Midolo, P. Lodahl, and N. Rotenberg, "An integrated whispering-gallery-mode resonator for solid-state coherent quantum photonics," arXiv, arXiv:2107.12188 [quant-ph] (2021).